

Seasonal tracer subduction in the Subpolar North Atlantic driven by submesoscale fronts

Théo Picard¹, Jonathan Gula², Clément Vic², Laurent Mémery ³

¹Univ Brest, CNRS, IRD, Ifremer, Laboratoire des Sciences de l'Environnement Marin (LEMAR), IUEM,

Plouzané, France

²Univ Brest, CNRS, IRD, Ifremer, Laboratoire d'Océanographie Physique et Spatiale (LOPS), IUEM,

Plouzané, France

³...

Key Points:

- Key points are limited to three and are short sentences with the main results (we can discuss them when we agree on a version of the manuscript).
- Submesoscale fronts
- Strain-vorticity JPDF
- Numerical model
- Passive tracer
- Subduction

17 **Abstract**

18 Submesoscale flows (0.1 - 10 km) are often associated with large vertical velocities, which
 19 can have a significant impact on the transport of surface tracers, such as carbon. How-
 20 ever, global models do not adequately account for these small-scale effects, which still
 21 require a proper parameterization. In this study, we introduced a passive tracer into the
 22 mixed layer of the northern Atlantic Ocean using a high-resolution ($\Delta x = 800$ m) CROCO
 23 simulation, aiming to investigate the seasonal submesoscale effects on vertical transport.
 24 Using surface vorticity and strain criteria, we identified regions with submesoscale fronts
 25 and quantified the associated subduction, that is the export below the mixed layer depth.
 26 Notably, we observed significant seasonal variations, with submesoscale fronts contribut-
 27 ing to 40% of the total tracer export in winter, which decreased to 1-2% in summer. Ad-
 28 ditionally, we suggest that tracer vertical distribution and the contribution of frontal sub-
 29 duction could be estimated from surface strain and vorticity.

30 **1 Introduction**

31 There is an on-growing set of evidence that submesoscale physical processes actu-
 32 ally matter for the transport of oceanic tracers such as heat, carbon and nutrients (Klein
 33 & Lapeyre, 2009; Omand et al., 2015; Stukel et al., 2017; Llort et al., 2018; Lévy et al.,
 34 2018; Boyd et al., 2019; Lacour et al., 2019). Submesoscale phenomena are characterised
 35 by frontal and filamentary structures with lateral scales ranging from 1 to 10 km. These
 36 structures typically arise from mesoscale eddy stirring and baroclinic instability at the
 37 ocean surface, exhibiting Rossby ($Ro = \zeta/f$) numbers on the order of 1 (Lévy et al.,
 38 2024). The frontogenesis, responsible for ageostrophic flow known as secondary circu-
 39 lation, induces strong and deep vertical velocities localised precisely at the front (McWilliams,
 40 2021; Gula, Taylor, et al., 2021). Fronts are characterised by a dense cyclonic side with
 41 downward velocities and a light anticyclonic side with upward velocities. In the context
 42 of the carbon cycle, this results in a double contribution : On the one hand, it drives nu-
 43 trients, essential for the primary production, from the (interior) twilight zone into the
 44 euphotic layer (Lapeyre Guillaume, 2006; Lévy et al., 2018; Mahadevan, 2016). On the
 45 other hand, it facilitates the subduction of surface carbon (transport below the mixed
 46 layer) along isopycnal pathways, effectively storing it for extended periods (Wenegrat et
 47 al., 2020; Mahadevan et al., 2020; Freilich & Mahadevan, 2021). Concerning heat trans-
 48 port, L. Siegelman et al. (2020) demonstrated that fronts actively participate to upward
 49 heat transport from the ocean interior to the surface and they are essential ingredients
 50 in the Earth's heat budget.

51 While it is clear that fronts play a significant role in tracer budgets, the vertical
 52 transports induced by submesoscale processes remain unresolved and are not yet param-
 53 eterized in climate models (Bopp et al., 2013; Mahadevan et al., 2020). Addressing this
 54 challenge represents one of the major hurdles in ocean modeling (Fox-Kemper et al., 2019).
 55 But if the quantification of submesoscale contributions to tracer transport has recently
 56 gained interest, there is still no clear consensus on its impact. One significant obstacle
 57 is the difficulty to sample submesoscale processes using remote sensing and in situ ob-
 58 servational instrumentation. Indeed, satellite altimetry can only detect structures larger
 59 than 100 kilometers (Chelton et al., 2011), and measuring the vertical transport due to
 60 small-scale phenomena in the ocean remains a challenge (Mahadevan et al., 2020). The
 61 computation of submesoscale gradients of velocity generally requires multiple ships, au-
 62 tonomous underwater vehicles, or surface drifters (Shcherbina et al., 2013; Gula, Tay-
 63 lor, et al., 2021). Regarding numerical simulations, it has been demonstrated that fine-
 64 scale ocean regional circulation models with subkilometer-scale horizontal grid spacing
 65 can accurately capture submesoscale dynamics (Mahadevan & Tandon, 2006; Capet et
 66 al., 2008; Pietri et al., 2021). However, high-resolution modeling often comes with com-
 67 putational cost limitations (Lévy et al., 2024), resulting in spatial restrictions and/or ide-
 68 alized setups.

Various methodologies have been proposed to assess the frontal contribution, particularly in the context of carbon export. Balwada et al. (2018) estimated that the subduction could double by comparing 20 and 1 km horizontal resolution model. Uchida et al. (2019) quantified the ageostrophic contribution using spectrum analyses and determined that submesoscale structures could account for approximately one-third of the total fluxes. In Freilich and Mahadevan (2021), Lagrangian particles were employed to identify particles trapped within submesoscale structures. Their findings revealed that 7.7% of the particles are subducted out of the mixed layer, with subduction primarily occurring in localized regions along fronts. Based on glider observations during the North Atlantic bloom and supported by numerical model, Omand et al. (2015) showed that submesoscale structures can contribute as much as half of the total springtime export of particulate organic carbon (POC). In a recent study, Balwada et al. (2021) employed Joint Probability Density Function (JPDF) of surface vorticity and strain on a fine scale model in the Antarctic Circumpolar Current to identify fronts. Their research revealed that submesoscale fronts, despite occupying only approximately 5% of the surface domain, could potentially account for as much as 20% of the vertical transport at the Mixed Layer Depth (MLD). This wide range of results underscores the complexity and the substantial uncertainties associated with this topic.

Despite this growing body of literature, a notable gap in knowledge exists as most studies tend to overlook the seasonal variability of these phenomena. Yet, it is now clear that submesoscales feature a strong seasonal cycle (Callies et al., 2015; Rocha et al., 2016; Berta et al., 2020). Moreover, the modulation of tracer export on seasonal time scales has been evidenced recently (Cao & Jing, 2022; Mahadevan et al., 2020). Hence, the primary objective of our study is to assess the seasonal impact of submesoscale processes on a passive tracer released in the mixed layer (ML) using a highly realistic model. We focus particularly on the North Atlantic subpolar gyre region, a region known for significant seasonal variations. Moreover, this region is particularly important as being one of the most critical areas for carbon sequestration, with an average uptake of approximately $0.7 \pm 0.1 \text{ Pg C year}^{-1}$ which constitutes $\sim 30\%$ of the global net ocean uptake (Takahashi et al., 2002; Olafsson et al., 2021) and with significant phytoplankton blooms in Spring, when submesoscale activity is intense (Treguier et al., 2005; Le Corre et al., 2020).

The outline of this paper is as follows. Section 2 introduces our numerical simulation. In section 3, we outline the methodology employed to identify seasonal surface submesoscale fronts. Section 4 describes the seasonal evolution of a tracer released within the ML and analyzes the contribution of fronts to tracer subduction. Finally, section 5 offers a detailed discussion of the results.

2 Methodology

2.1 Numerical setup

We set up a realistic simulation of the circulation in a north-east portion of the North Atlantic subpolar gyre, using the oceanic modeling system CROCO (Coastal and Regional Ocean COmmunity model) that resolves the primitive equations (Shchepetkin & McWilliams, 2005). A nesting approach is chosen here using GIGALT3 as the parent simulation, which is a realistic simulation that covers most of the Atlantic Ocean with a horizontal resolution of 3 km (Gula, Theetten, et al., 2021). GIGALT3 provides the nested simulation with the initial state and the lateral boundary conditions. The study domain is illustrated in Figure 1, covering an area of $800 \text{ km} \times 640 \text{ km}$, ranging from 53.8°N to 62.5°N and from 20.5°W to 37.8°W . The horizontal grid spacing $\Delta x = 800 \text{ m}$ is almost constant over the domain. Vertically, we discretize the model with 200 sigma levels, which roughly corresponds to cell heights of $\Delta z = 2 \text{ m}$ within the surface layer. This vertical resolution is chosen to accurately represent the surface dynamics. The ocean is forced

at the surface by hourly atmospheric forcings from the Climate Forecast System Reanalysis using a bulk formulation with relative winds (Saha et al., 2010). Tidal forcing is not included. The grid bathymetry is from the global SRTM30plus data set (J. J. Becker D. T. Sandwell & Weatherall, 2009). The simulation, named RREX2008 (Reykjanes Ridge Experiment), is run for 13 months, from December 1, 2007, to December 31, 2008, with a time step of 90 seconds and 3-hour averaged output intervals. The first month is dedicated to the spin-up phase, ensuring that submesoscale structures become prominent in our numerical simulation. We thus analysed the outputs for year 2008.

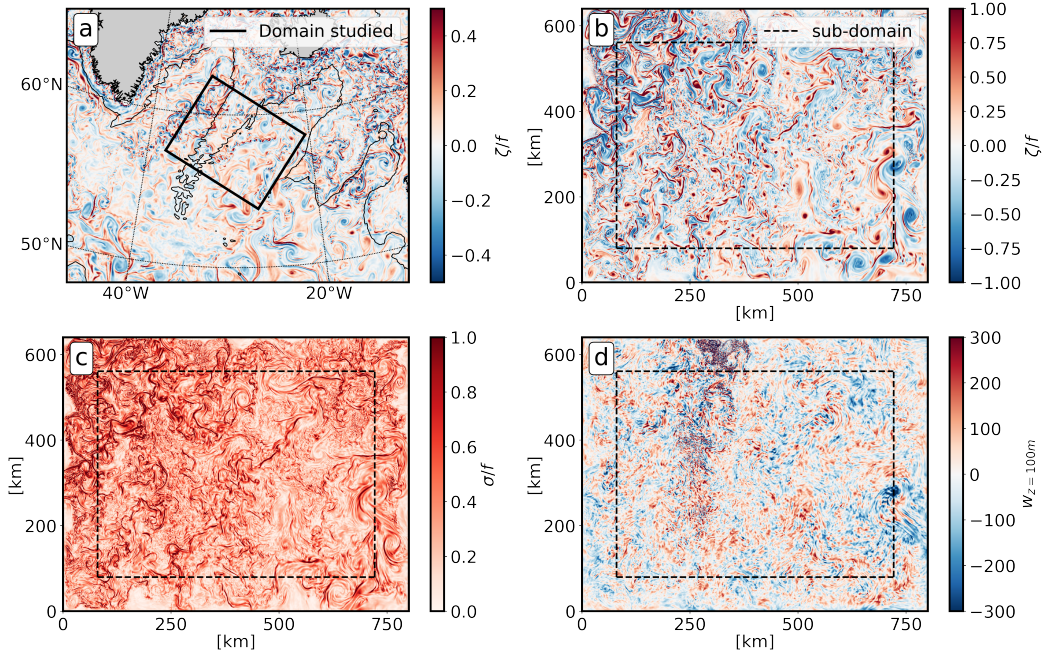


Figure 1. (a) Snapshot of the GIGATL3 simulation ($dx = 3\text{km}$) the 8th of February . The background is the relative vorticity and black contour is the bathymetry at 2000 m. The black rectangle is the domain of the RREX2008 simulation. (b), (c) and (d) represent respectively the relative vorticity, the strain and vertical velocities at 100 m depth computed from RREX2008 simulation ($dx = 800\text{m}$). The relative vorticity and strain are normalised by the local Coriolis frequency. All the statistical results are computed in the dashed rectangle sub-domain to discard boundary effects.

2.2 Tracer initialisation and equation

On the first day of each month, a passive tracer is released throughout the entire domain within the upper mixed layer (ML) and remains for a period of 29 days. This experimental design enables us to evaluate and compare both ML water subduction and deep export for each month independently. The MLD is determined by computing a density threshold of 0.03 kg m^{-3} from the surface, as described in de Boyer Montégut et al. (2004). We distribute the tracer concentration C following a hyperbolic tangent profile:

$$C(x, y, z, t = 0) = \frac{1}{2} \left(1 + \tanh \left(\frac{z - z_{target}}{dz(x, y)} \right) \right) \quad (1)$$

135 Where x, y, z represent the spatial coordinates, and t is time. We choose $z_{target} =$
 136 $0.6 \cdot z_{mld}(x, y)$ to ensure that there is no tracer below the MLD. Additionally, $dz = \frac{-z_{mld}(x, y)}{8}$
 137 is chosen to achieve a smooth transition near the MLD to avoid numerical instabilities
 138 due to sharp vertical gradients of tracer concentration. Figure 2 provides an example of
 139 the tracer concentration for 3 selected days in February. It illustrates how the tracer is
 140 stirred by the mesoscale and submesoscale circulation and how it accumulates or is de-
 141 pleted from frontal regions.

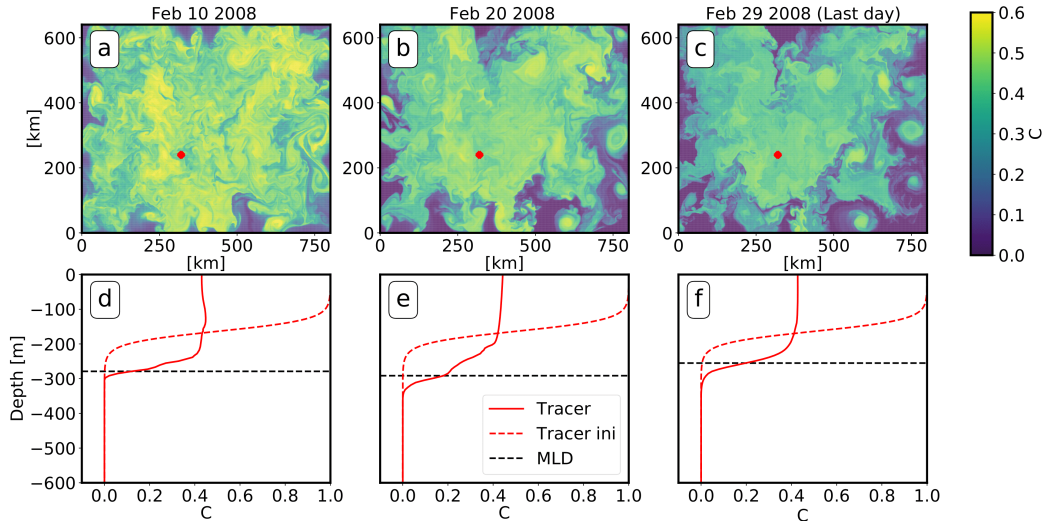


Figure 2. (a), (b) and (c) represent the tracer concentration at the surface for February 10, 20 and 29. (d), (e) and (f) show the corresponding tracer vertical distribution (red line) for the red cross location. The dashed red line shows the tracer initial vertical distribution and dashed black line is the MLD.

142 The CROCO model uses the following tracer equation:

$$\frac{\partial C}{\partial t} = -u_j \frac{\partial C}{\partial x_j} - w \frac{\partial C}{\partial z} + \nu_c + D_c + S_c \quad (2)$$

143 Where C represents the tracer concentration, u_j correspond to the horizontal ve-
 144 locities, w the vertical velocity, ν_c is the vertical diffusion, D_c is the horizontal diffusion
 145 and S_c is a source term (set to zero in this study). D_c is not explicit in CROCO but arises
 146 from the implicit contribution of the upstream-biased advection scheme. Vertical mix-
 147 ing ($\nu_c = \frac{\partial}{\partial z} (K_c \frac{\partial C}{\partial z})$) computed with the diapycnal diffusivity K_c is parameterized with
 148 the KPP scheme (Large et al., 1994).

149 3 Seasonality of submesoscale fronts

150 The numerical simulation provides compelling evidence for tracer subduction driven
 151 by fronts. Figure 3 presents a vertical section of the domain on April 3rd, i.e., 3 days af-
 152 ter tracer release. The vertical cross-section highlights a distinct front characterized by
 153 significantly enhanced vertical velocity ($w > 100$ m/d) and a noticeable tracer subduc-
 154 tion below the mixed layer. In this section, we first explain how we identify submesoscale
 155 fronts based on a strain and vorticity criterion and we present a first analysis to quan-
 156 tify the seasonal variations in the prevalence of fronts and their associated velocity field.

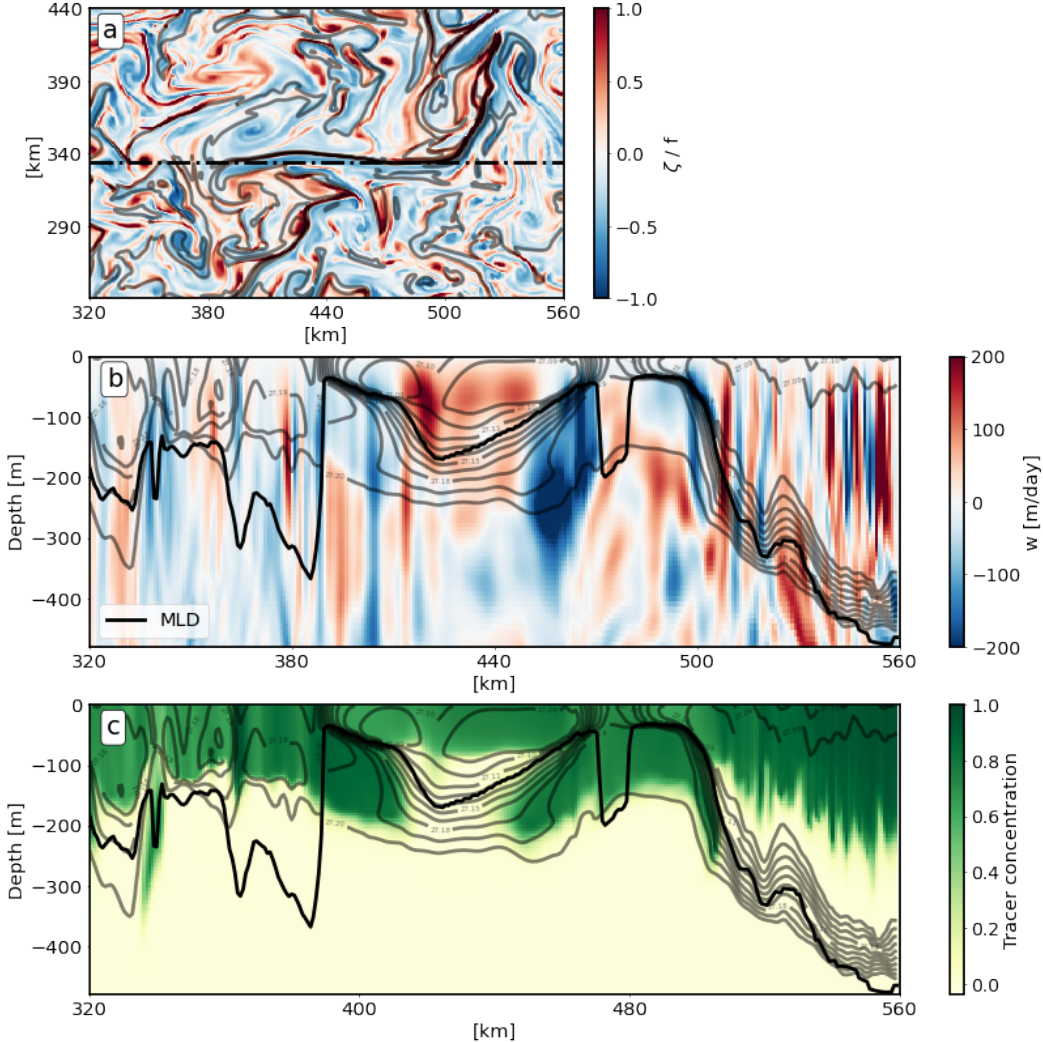


Figure 3. (a) Snapshot of the surface relative vorticity the 3rd of April. The vertical section over a front is marked with a dashed black line. (b) Vertical cross section. Colors represent vertical velocities. The black line is the mld computed with a density threshold. The grey lines are the isopycnals. c) Tracer concentration on the same vertical section.

157

3.1 Seasonal variability of submesoscale fronts

158
159
160

The dynamics of the horizontal flow can be expressed with the strain tensor. This strain tensor can be decomposed into the vertical vorticity ζ , horizontal divergence δ and strain rate σ (called strain to simplify in the following) such as :

$$\zeta = \frac{\partial v}{\partial x} - \frac{\partial u}{\partial y} \quad ; \quad \delta = \frac{\partial u}{\partial x} + \frac{\partial v}{\partial y} \quad ; \quad \sigma = \sqrt{\left(\frac{\partial u}{\partial x} - \frac{\partial v}{\partial y}\right)^2 + \left(\frac{\partial u}{\partial y} + \frac{\partial v}{\partial x}\right)^2} \quad ; \quad (3)$$

161
162
163
164

Strain and vorticity are commonly used to identify structures such as submesoscale fronts and eddies. Figure 1 displays the vorticity and strain within the domain on 8th February. During this winter period, we observe widespread and intense submesoscale structures, including filaments characterized by high vorticity and strain. This signature

distinguishes them from eddy structures, which typically exhibit significant vorticity but weak strain patterns (Gula et al., 2014). Hence, a flow decomposition based on joint probability density functions of surface vorticity and strain proves valuable to identify fronts and eddies (Shcherbina et al., 2013). Previous studies used the vorticity-strain space to localize submesoscale fronts within regions close to the lines $\sigma = |\zeta|$ (Shcherbina et al., 2013; McWilliams, 2016; Balwada et al., 2021). In turbulent regime ($|\delta| \sim |\zeta|$; Gula et al. (2014)), Barkan et al. (2019) demonstrated that fronts tend to aggregate around the lines $\sigma = \sqrt{2}|\zeta|$. However, to our knowledge, none of the previous studies have precisely defined the area that corresponds to submesoscale fronts. Consequently, we have chosen to define a frontal region characterized by $\sigma > |\zeta|$ and with a restrictive criterion $|\zeta/f| \sim Ro > 0.5$. The Ro criteria is based on the work of L. I. Siegelman (2020), who observed in fine resolution model that submesoscale structures above the permanent thermocline characterised by ageostrophic flow are associated with $Ro > 0.5$. With mooring observations, Buckingham et al. (2016) estimated $|Ro|$ values of 0.3–0.45 at scale 1.5 km in a quiescent region in the North Atlantic. We define two sub-domains, labeled 1A delimited by dots and 1C identified by hatches, corresponding respectively to the submesoscale fronts for anticyclonic and cyclonic fronts (Figure 4). It is worth noting that separating cyclonic and anticyclonic fronts is meaningful, as cyclonic fronts (1C) are known to contribute significantly to intense downward velocities, while anticyclonic fronts generally induce upwelling and weaker velocities (Gula, Taylor, et al., 2021). Additionally, we name the two other zones based on Balwada et al. (2021): the anticyclonic zone (2) defined by $\zeta/f > 0$ and $\sigma < |\zeta|$, and the cyclonic zone, defined by $\zeta/f < 0$ and $\sigma < |\zeta|$. These regions correspond to points within eddies.

Figure 4a displays the integrated surface strain-vorticity JPDF computed over March 2008. These statistics are computed within bins of size of 0.05×0.025 (vorticity \times strain). The contour line delineates the region embedding 99.99% of the grid points. It is noteworthy that a major portion of surface points exhibit weak vorticity and strain ($\zeta/f < 0.5$ and $\sigma/f < 0.5$), in coherence with the quasi-geostrophic regime of turbulence expected to develop at this model resolution. The observed asymmetry, characterised by a peak in 1C, represents the signature of submesoscale fronts (McWilliams, 2016; Buckingham et al., 2016). The 99.99% contour of surface vorticity-strain JPDF is shown for each month in Figure 4b). Each season exhibits a distinct JPDF signature, reflecting a clear evolution in shape driven by the presence of submesoscale dynamics. Because of more energetic submesoscales at the surface (Callies et al., 2015), the winter period features the largest domain with the highest asymmetry, while the JPDF envelop in the summer months is confined to a region of small strain and vorticity. Interestingly, during spring, the peak remains significant, making this period particularly relevant for organic carbon export, as the region hosts significant phytoplankton blooms in the euphotic layer. To quantitatively assess the presence of fronts, we calculate the fraction of points within regions 1A + 1C for each month, which we consider as the front density (Figure 5a). The front surface fraction is maximum in March, accounting for about 9% of the total surface (5.7 % in 1C). Conversely, the lowest fraction of submesoscales is found in July with less than 0.5%.

3.2 Seasonal variability of vertical velocity

Following the approach in Balwada et al. (2021), which assumes that some variables at depth are constrained by the surface dynamics, we look at the distribution of some variables at depth as a function of surface vorticity and strain. This hypothesis reveals interesting patterns of the vertical velocity w . For each month, we computed the distribution of the bin-averaged vertical velocity $\langle w_z \rangle$, conditioned on surface vorticity and strain over 20 vertical z levels equally spaced from the surface to $2 \times \text{MLD}$. An example is provided for March in Figure 6. Similar to the density JPDF, we use 3-hour outputs (averages) during the first 29 days of each month. Our approach is akin to that of Balwada et al. (2021), with a key difference being that instead of considering a hor-

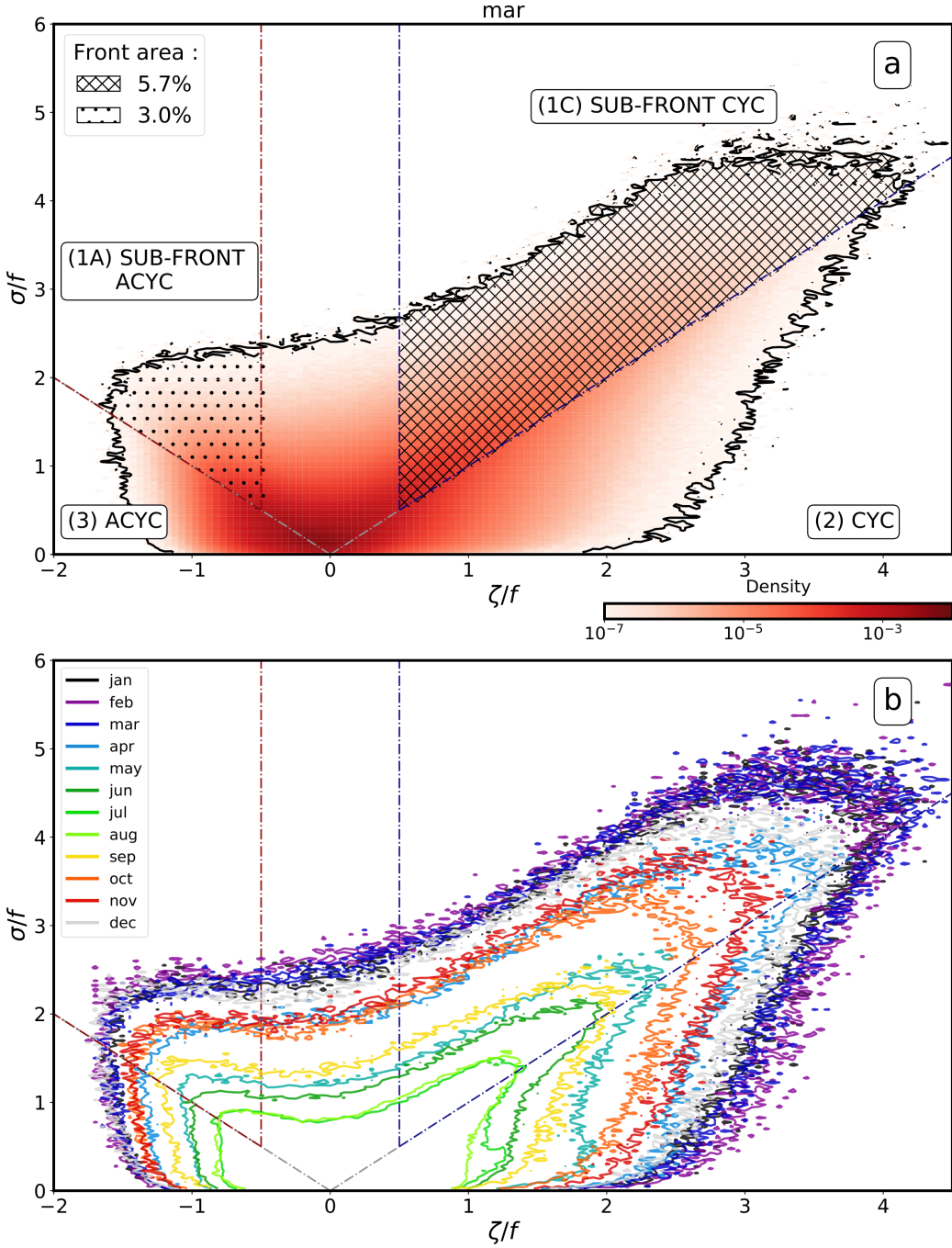


Figure 4. (a) Surface strain - vorticity JPDF in March. The black contour is the integrated domain that contain 99.99% of points. (1A) is the anti-cyclonic submesoscale front zone and (1C) is the cyclonic submesoscale front zone. (2) and (3) are respectively the cyclonic and anticyclonic zones. The fraction of points inside 1A (dotted area) and 1C (hatched area) are given. (b) Surface strain - vorticity JPDF domain contours (99.99% of the points) for each month.

218 horizontally constant MLD, we compute the MLD at each grid point and for each time step.
 219 We notice that the cyclonic part is generally associated with $\langle w \rangle < 0$. The largest neg-
 220 ative velocities are located inside the 1C area and is persistent with depth down to $2 \times MLD$.

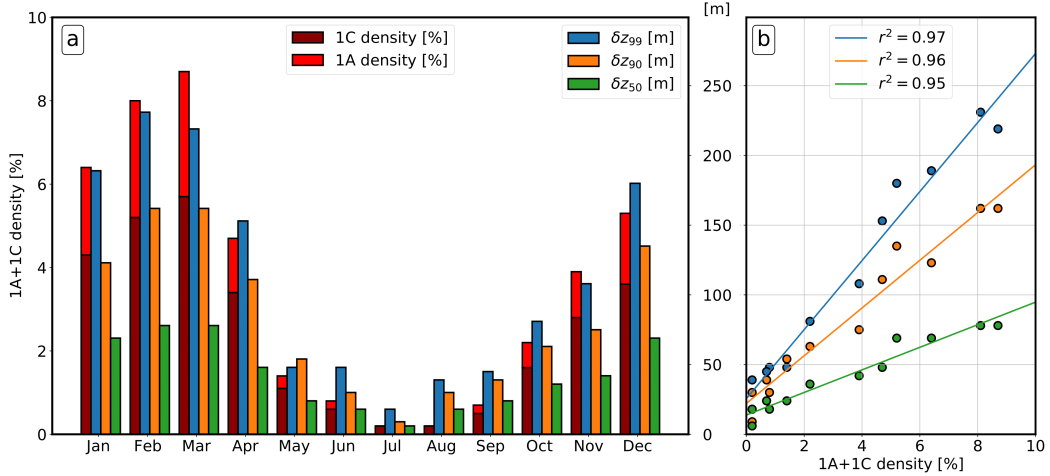


Figure 5. a) Deepening of the 50th (green), 90th (orange) and 99th (blue) tracer percentile between the first and last day for each month experience. Red bars is the fraction of points inside 1A and 1C. b) Linear regression between front density and tracer deepening.

For the anti-cyclonic area, $\langle w \rangle$ is generally positive near the surface regardless of fronts or eddies. However, we observe a shift in the sign of the velocities in 1A close to the MLD and below. This shift is a direct consequence of the methodology limit. Indeed, the dynamics conditioned at depths, especially below the MLD, may not always be directly linked to surface properties. First, the effects of fronts are only localised near the surface and it is possible that the second circulation associated does not match the MLD and below. Additionally, vertical velocities induced by a front often follow isopycnal pathways, which are not vertical and include horizontal component (Freilich & Mahadevan, 2021). Consequently, the subduction associated may not necessarily be located directly beneath its apparent surface signature, and lateral advection transport may also be induced. This is particularly an issue for the light anticyclonic side of front whose upward pathway can be located above the dense cyclonic downward pathway (Figure A1). Consequently, below a certain depth, we are associating a part of the cyclonic downward velocity with the 1A area, biasing the results, especially with month associated with deep MLD like March.

Focusing in the frontal areas, we compare monthly results in the water column with the depths relative to the MLD. We compute the density-weighted mean $\langle w_z \rangle$ (i.e the mean velocities weighted with the corresponding bin-density) for 1C and 1A over the vertical (Figure 7a,b). The maximum velocities within fronts are typically observed at depths equivalent to $0.3\text{--}0.4 \times \text{MLD}$ and usually fall to much weaker value close to the MLD. 1C is consistently associated with downwelling, displaying varying seasonal intensities ranging from -130 m/day (Winter) to -10 m/day (Summer). In contrast, region 1A exhibits upwelling with values ranging from 70 m/day to 5 m/day . It is important to note that below the MLD, $\langle w \rangle$ in 1C consistently remains negative, while for 1A, $\langle w \rangle > 0$ above $1.1 \times \text{MLD}$. From October to March, which are month associated with deep MLD, we observe a transitions from positive to negative values below $1.1 \times \text{MLD}$ due to the bias mentioned before.

To quantify monthly subduction, we particularly focus on the mean vertical velocity at the MLD ($\langle w_{\text{mld}} \rangle$) Figure 8. Although there is a monthly variability of the distribution of $\langle w_{\text{mld}} \rangle$, we still observe a consistent pattern in vertical velocity. Notably, both anticyclonic (3) and cyclonic (2) features are associated with positive vertical ve-

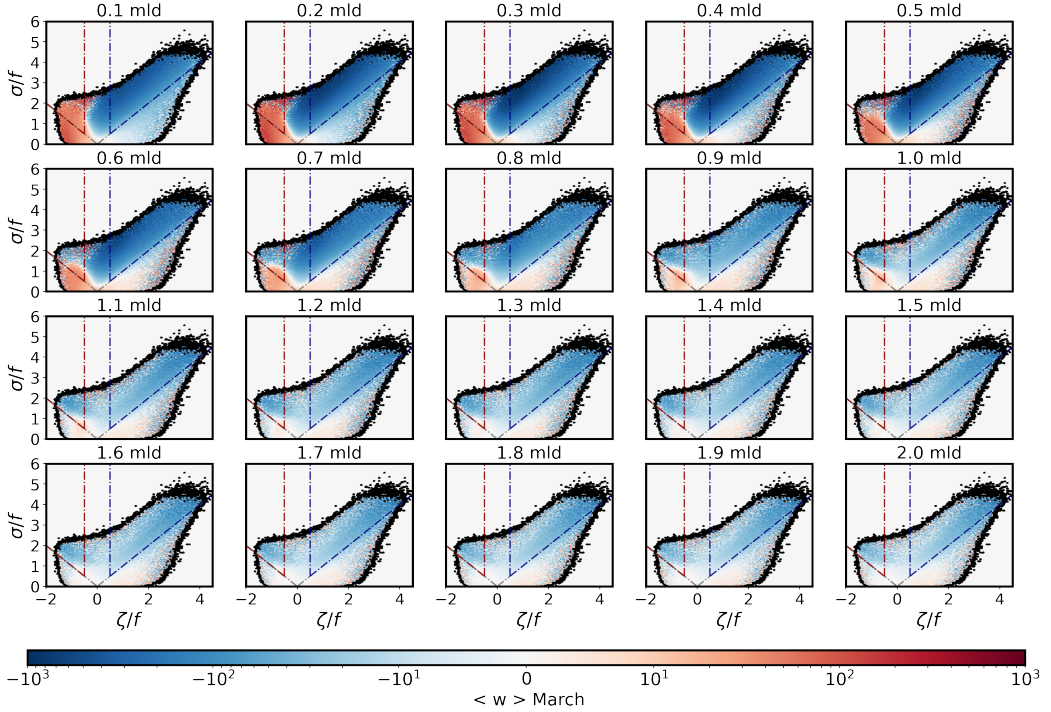


Figure 6. Bin-averaged vertical velocity conditioned on surface vorticity and strain at different vertical levels during March. Black contour is the integrated domain that contain 99.99% of points. The remain 0.01% points are hidden.

locities. Cyclonic fronts in region 1C exhibit strong downward velocities, while region 1A displays a mix of positive and negative vertical velocities. Excepted for the 1A area, we notice robust w patterns constrained with surface dynamical characteristics regardless the seasons and the depths. This observations support our assumption that surface dynamics drive most of the vertical velocity at the MLD. At first sight, the mean vertical velocity seems to follow a seasonal pattern. The relation between the front area density and $\langle w_{mld} \rangle$ in 1A and 1C are presented in Figure 7c,d. It shows moderate correlation with $r^2 = 0.37$ in 1C and $r^2 = 0.54$ in 1A (Taylor, 1990; Ratner, 2009), which suggest at first glance that vertical velocities are more intense at the MLD when front density is significant.

4 The seasonal tracer evolution

4.1 Tracer deepening

We examine the tracer evolution over the vertical in Figure 9, which displays the average tracer concentration within 3-meter bins and the spatially averaged evolution of the mixed layer depth $\langle MLD \rangle$. Over the study period, the ML has a typical seasonal evolution characterised by a stable and large depth in winter, intense spring stratification, a shallow and stable depth in summer and a gradual deepening in fall. To estimate the tracer's evolution more effectively, we compute the distribution of tracer concentration as a function of depth and monitore the distribution's median, 90th, and 99th percentiles. For each month, the tracer spreads deeper into the water column, and the concentration within the ML decreases. It is important to note that since the simulation has open boundaries, the tracer can escape through the boundaries, but this does not im-

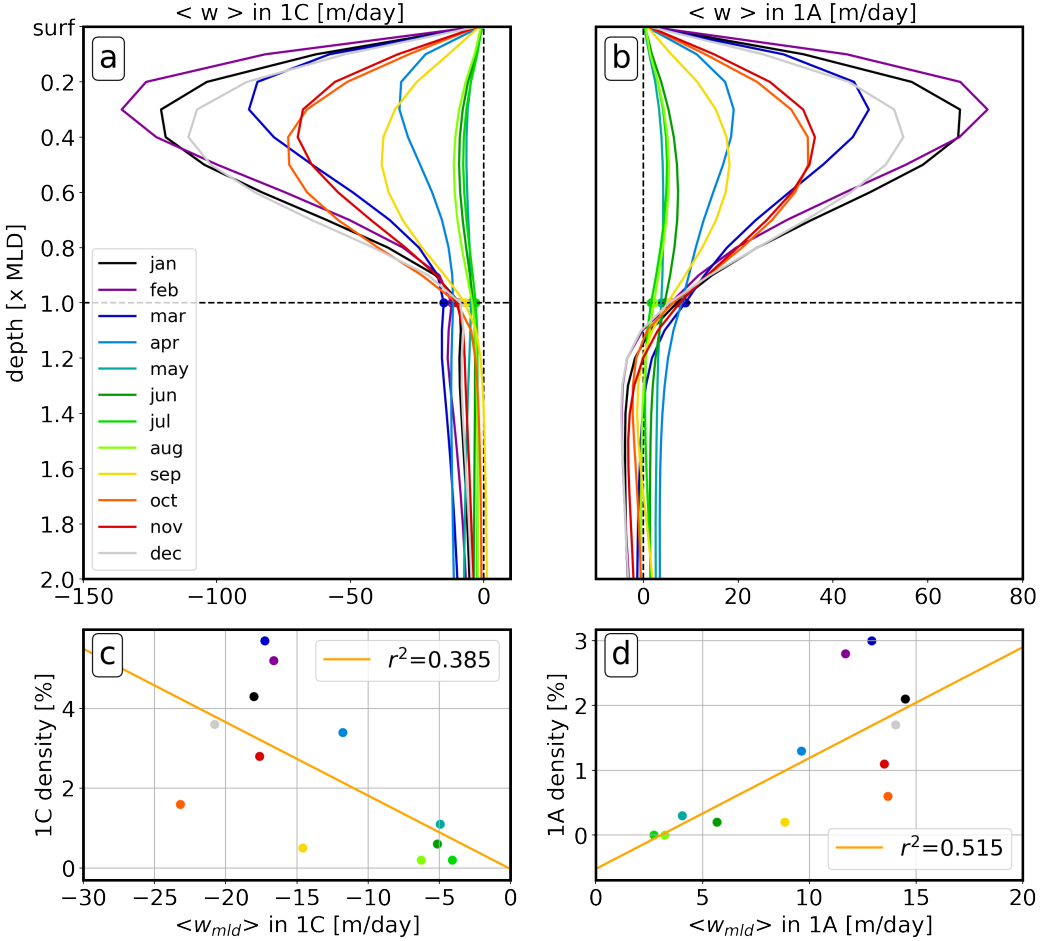


Figure 7. Vertical velocity mean $\langle w \rangle$ in the 1A (a) and 1C (b) area between the surface and $2 \times \text{MLD}$ for each month. Linear regression between the mean velocity at MLD $\langle w_{mld} \rangle$ and the front density in 1A and 1C.

pact the statistical results. The tracer depth is particularly important for carbon export since the carbon sequestration time directly depends on the depth of injection (Bol et al., 2018). The difference between the depth of each percentile on the first day and on the last day ($\delta z_{99}, \delta z_{90}, \delta z_{50}$) is plotted in Figure 5a). The varying seasonal conditions allowed us to compute the linear regression between the front density and the tracer deepening. Interestingly, $\delta z_{99}, \delta z_{90}$ and δz_{50} appear to be significantly correlated with the front density (Figure 5b). This suggests that the front density could impact the depth at which the tracer is subducted. Consequently, surface conditions can potentially serve as an indicator for estimating the redistribution of tracer at depth in this region.

4.2 Seasonal tracer subduction driven by submesoscale fronts

To estimate the submesoscale fronts contribution to tracer vertical transport, we mapped the vertical transport of the tracer, (wC) in surface strain-vorticity space – w represents the vertical velocity, and C is the tracer concentration. We computed the sum ΣwC inside each bin and similarly to part 3.3, these results are computed for 20 vertical levels between the surface and $z = 2 \times \text{MLD}$. An example with March is given Figure 10. Inside the mixed layer, the transport is similar to what we observe with veloc-

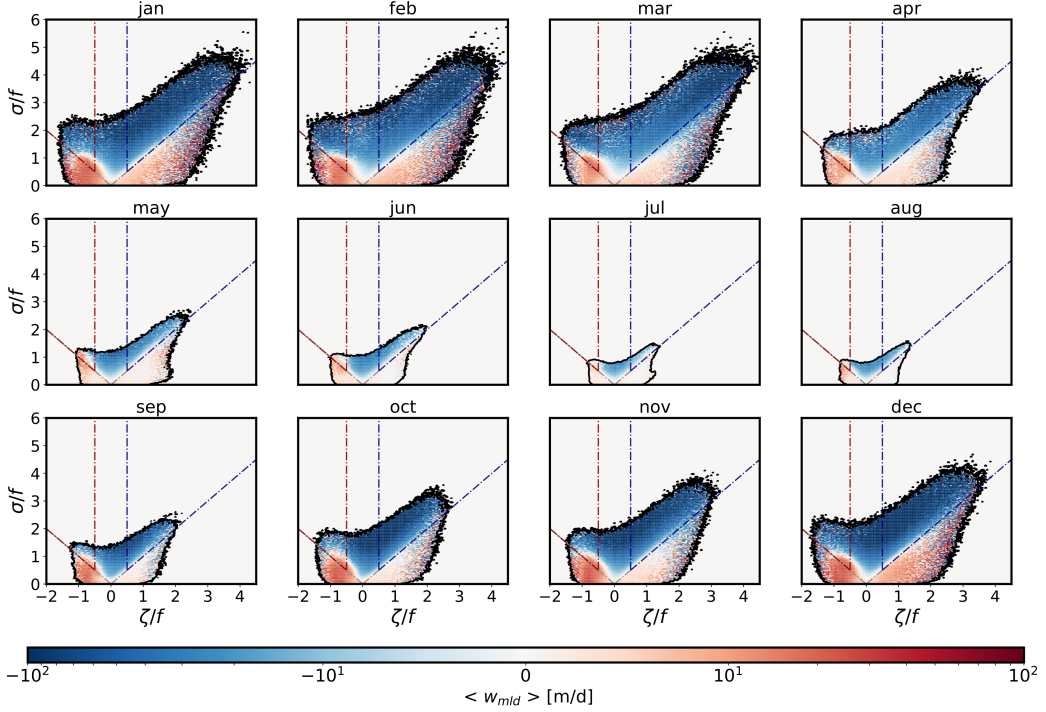


Figure 8. Surface strain-vorticity JPDF conditioned with the mean vertical velocity w at mld and for each month. Black contour is the integrated domain that contain 99.99% of points (points outside have been removed).

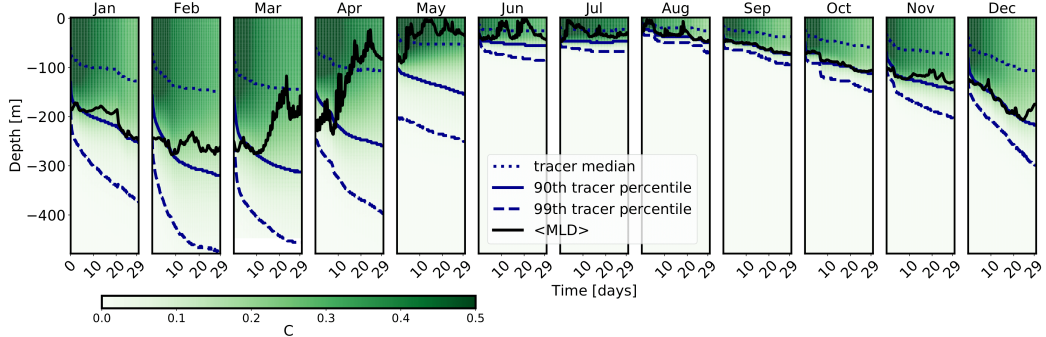


Figure 9. Tracer distribution and evolution for each month. The tracer concentration is vertically averaged over 3-meter bins. The black line is the spatial mean of the mixed layer depth computed for every time step (3h) with a density threshold. Blue lines represents the 50th (dotted), 90th (solid) and 99th (dashed) percentile of the tracer.

ity Figure 6. This is because the tracer is mostly uniform over the mixed layer and always positive. Hence, the total transport is directly linked with the mean velocity. However, below the MLD, the transport is mostly negative in every area. This is because no tracer where injected at this depth during the initial conditions. A small part in eddies region still present positive transport, suggesting that a part of subducted tracer can be re-injected in the mixed layer during the month inside this region. The blue contours indicate the region contributing to respectively 50% and 99% of downward transport. It is clear that most of the downward contribution is associated with small strain and vor-

298 ticity, where the density is maximum 4. But the 1C area seems to be as well a significant
299 region to participate in export.

300 To confirm this trend, for each month and within the depth range between the sur-
301 face and $2 \times \text{MLD}$, we calculate inside 1A and 1C both the total tracer fluxes, i.e., the
302 sum of the bins in 1A and 1C (Figures 11a and b). We also estimated the proportion
303 of these fluxes relative to the overall downward fluxes, i.e., $\frac{\Sigma wC_{1C}}{\Sigma wC_{wC < 0}}$ and $\frac{\Sigma wC_{1A}}{\Sigma wC_{wC < 0}}$ (Fig-
304 ures 11c and d). Similarly with w , the transport wC in 1C and 1A reach a peak at $z =$
305 0.3-0.4 MLD and decrease significantly close to the MLD. In 1C, the transport remain
306 always negative and can contribute significantly to the total downward transport between
307 the surface and $2 \times \text{MLD}$. However in 1A, the positive transport sign shift precisely
308 at the MLD and become negative below. It is challenging to interpret the results in 1A
309 below the MLD. Since no tracer were injected below the MLD, positive contribution can't
310 be significantly observed. Additionally, the negative export in this region can be also due
311 to the bias mentioned section 3.2.

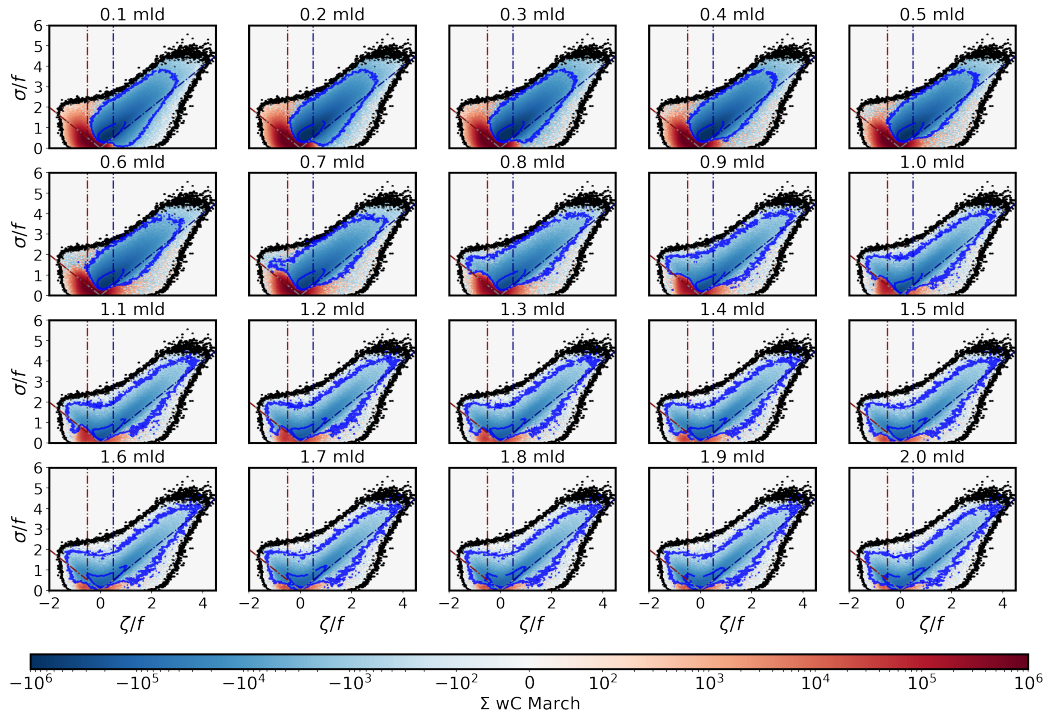


Figure 10. Surface strain-vorticity JPDF conditioned with the sum of vertical transport ΣwC at different vertical levels for March. Black contour is the integrated domain that contain 99.99% of points and points outside have been removed. Blue contours contain the integrated points contributing to 50% (inside) and 99% (outside) of the total downward transport.

312 Focusing on the subduction, we plotted $w_{\text{mld}}C_{\text{mld}}$ conditionned on vorticity-strain
313 for each month Figure 12. Regardless of the seasons, the anticyclonic area (3) and cy-
314 clonic area (2) contribute primarily to upward transport, while the remaining region is
315 associated with predominantly downward transport. Again, we observe the important
316 contribution of the 1C area that essentially participate to downward fluxes. On the op-
317 posite, the figure shows in 1A positive transport close to the anticyclonic eddy border
318 and negative transport for intense strain that compensate each other as suggest Figures
319 11 b).

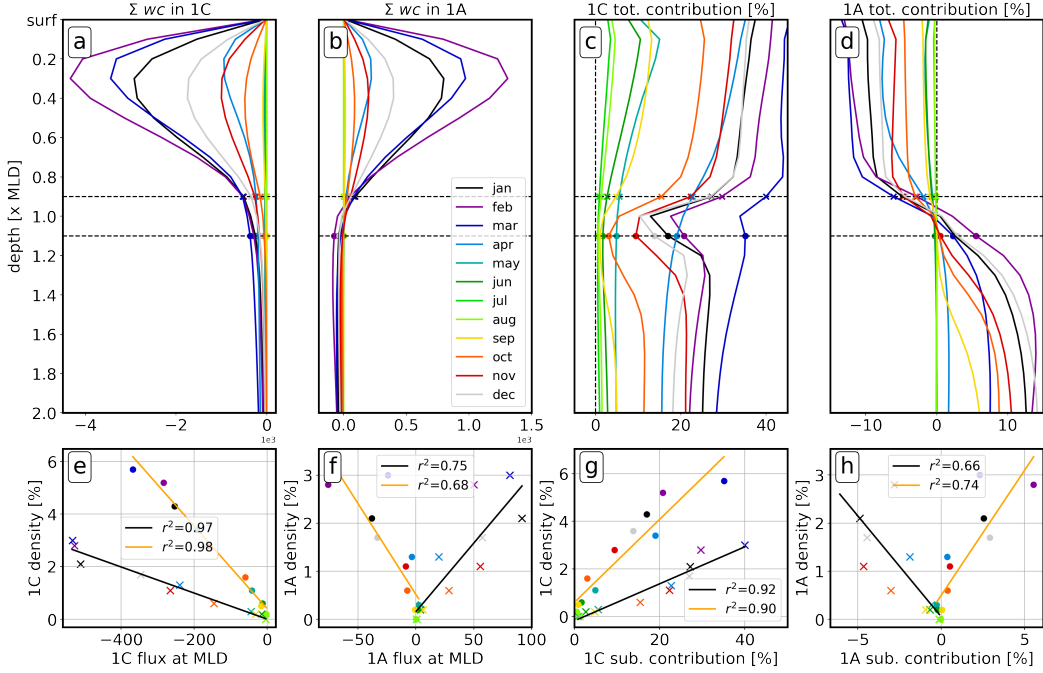


Figure 11. Net fluxes in 1C (a) and 1A (b) between surface and $2 \times \text{MLD}$. Contribution of total negative flux for 1C (c) and 1A (d). Corresponding linear regression between front area and fluxes at MLD / total subduction contribution are given for 1C (e,g) and 1A (f,h).

At the MLD, we observe a singularity in Figures 11 c) and d). This is due to the total downward fluxes (not shown) that present a local extremum at this depth. For the moment, this maximum is not fully understood. Hence, we decide to focus at the two depths 0.9 MLD and 1.1 MLD for a more robust description. As mentioned earlier, in 1A, we observe a shift in the sign of ΣwC , going to positive (i.e. obduction) to negative (i.e. subduction). Overall, the net flux close to the MLD are close to 0, indicating that 1A does not significantly contribute to subduction, the absolute contribution accounting for 1-5%. Conversely, the fluxes associated with 1C at the MLD are important and represent a significant contribution in terms of subduction, particularly during the winter and spring months with contribution accounting for 30-40% of the total flux. There is a slight decrease of the contribution with depth that again could be due to the limits of the methodology. We set the evidence of a clear link between the tracer fluxes, subduction contribution around the MLD, and the front density (Figures 11e-h). Specifically, the subduction contribution in 1C exhibits a direct correlation with the front density ($r^2 = 0.90 - 0.92$). The linear relation is also observed for the anticyclonic front, but not as effective ($r^2 = 0.66 - 0.74$). This results suggests that in this region, the frontal contribution and flux associated can be estimated from the strain-vorticity front surface signature.

5 Discussion

5.1 Bias and future improvements

Few studies have used surface strain-vorticity statistical tools to characterise submesoscale dynamics in both observations and models (Shcherbina et al., 2013; Rocha et al., 2016; Balwada et al., 2021; Vic et al., 2022). To our knowledge, Balwada et al. (2021) is the sole study using JPDFs and tracer vertical transport conditioned on surface strain

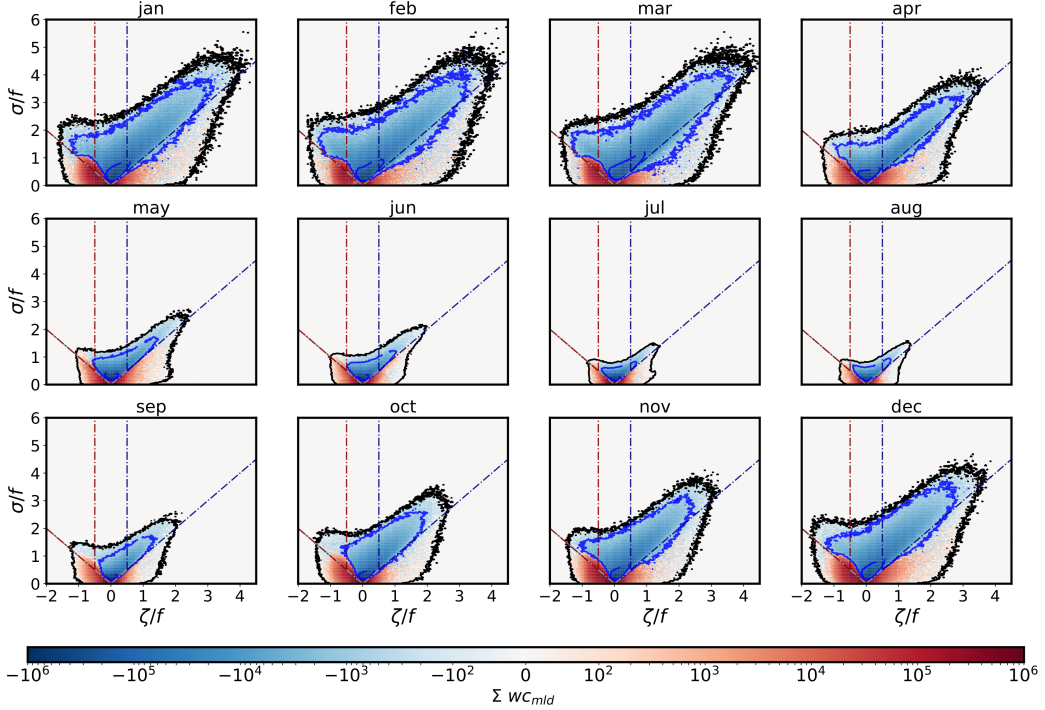


Figure 12. The sum of vertical advection $\Sigma w_{mld} \cdot C_{mld}$ conditionned with surface vorticity strain. Integrated blue contours indicated respectively 99% and 50% of the total negative flux. Black contour contain 99.99% of the points (points outside were hidden).

and vorticity to estimate the submesoscale front contribution at depth. However, it is important to note that results from numerical simulations can be highly sensitive to the grid resolution (Balwada et al., 2021) and the output frequency. In Figure A2, we compared the JPDF and the 1C density during the first 5 days of March with different output frequencies. The figure shows significant difference between daily-averaged (1.6 of cyclonic front density) and hourly-averaged or snapshot outputs (> 5 of cyclonic front density). Due to numerical storage constraints, we opted to use 3-h averaged outputs but it is worth mentioning that these outputs slightly smoothed the front impact compared to hourly snapshots resulting in a 0.5% loss of density. Therefore, our results may underestimate the front impacts on tracer transport. But as mentioned section 3.2, the main limitation of this methodology comes from the link between the surface associated with the dynamic at depth. Particularly, vertical velocities induced by a front are limited in depth and are not always following a 1D vertical direction. This result in a bias which may depends on depth and needs to be properly quantified in order to better understand the limited zone where such method can be used. This implied to detect with precision the frontal isopycnal pathways, which is a challenging task that still needs to be addressed.

Finally, the definition of the submesoscale front domains 1A and 1C used here are based on simplified assumptions. While this region provides a reasonable approximation to estimate the initial impact of submesoscale fronts, it requires further refinement. In reality, the surface submesoscale frontal area is more complex and may depend on the dynamics itself. Buckingham et al. (2016) demonstrated that ζ values in submesoscale regions are influenced by the Coriolis frequency and by the ratio of lateral and vertical buoyancy gradients. The Ro criteria used in our study may not be fully adapted in certain regions, such as the Gulf Stream, where Ro is approximately 0.7–1.0 within the sub-

369 mesoscale, exceeding our region's values. Therefore, we highlight the need for further theoretical development to precisely define a submesoscale zone within the surface strain-vorticity space. This will be crucial in the future for accurately estimating tracer export
 370 influenced by submesoscale dynamics.
 371

373 Yet, compared with previous studies, we observe similar associations between surface properties and transport at the MLD and we also find similar orders of magnitude
 374 in terms of submesoscale contributions, enforcing our confidence in the results.
 375

376 5.2 Toward a better parameterization of the effect of fronts on tracer 377 subduction

378 The main objective of this study is to gain a better understanding of the contribution
 379 of fronts to water subduction with a seasonal perspective. Properly quantifying
 380 subduction is crucial for understanding complex ocean mechanisms such as the carbon
 381 pump and heat transfer. Our seasonal study has allowed us to clearly identify front
 382 signatures and evaluate their impact on the transport of upper-layer water to depth. Signif-
 383 icant variations in front density enables us to hint a parameterization of the impact
 384 of fronts on tracer transport based solely on their surface characteristics. One important
 385 result is that the advective subduction contribution can be directly estimated from the
 386 surface dynamics. So far, satellites have not had the capability to detect submesoscale
 387 features (Ballarotta et al., 2019). However, with the ongoing Surface Water and Ocean
 388 Topography (SWOT) mission (Fu & Ubelmann, 2014), it will soon be possible to im-
 389 prove the altimetry resolution to 10-30 km. This will allow for better detection of front
 390 density and associated subduction rates, which is particularly relevant for biogeochem-
 391 ical studies focusing on the contribution of submesoscale features to the biological car-
 392 bon pump, often referred to as the eddy-subduction pump (Boyd et al., 2019). Subme-
 393 soscale processes capable of injecting particles to depth have not been quantified clearly
 394 yet, and this could partly explain why the mesopelagic ecosystem's demand for carbon
 395 exceeds the downward flux of presumably sinking POC by a factor of 2-3 (Burd et al.,
 396 2010). While this study used a simplified approach with homogenized tracer initializa-
 397 tion within the ML, the same methodology could be adapted to study the front's con-
 398 tribution to carbon export and nutrient injection using coupled biochemical modeling.
 399 Additionally, it is important to note that the seasonal results presented here are based
 400 on one year of data, and inter-annual variations can be significant (Berta et al., 2020).
 401 Further studies are needed to assess sensitivity associated to different time periods, re-
 402 gions, and numerical models.
 403

6 Conclusion

404 The present study investigates the seasonal fate of a passive tracer released each
 405 month within the surface mixed layer using a realistic high-resolution simulation in the
 406 North Atlantic. Employing surface strain and vorticity criteria, we identified and quan-
 407 tified front areas for each month in 2008. Our observations revealed a deeper descent of
 408 the tracer in the presence of submesoscale activities. Additionally, we estimated that cy-
 409 clonic submesoscale fronts occupy approximately 0.5% (summer) to around 6% (winter)
 410 of the domain and contribute respectively to about 0.5-40% of the total vertical advec-
 411 tive subduction. Overall, we identified a clear correlation between front density and tracer
 412 deepening / subduction rates. The findings of this study contribute to an enhanced un-
 413 derstanding of water subduction due to fronts and provide insights for the development
 414 of a submesoscale parameterization for global models.

415 **Acknowledgments**

416 T.P. received a Ph.D. grant from École Normale Supérieure Paris-Saclay. This work
 417 was also supported by the ISblue project, an Interdisciplinary graduate school for the
 418 blue planet (ANR-17-EURE-0015), and co-funded by a grant from the French govern-
 419 ment under the program "Investissements d'Avenir".

420 **References**

- 421 Ballarotta, M., Ubelmann, C., Pujol, M. I., Taburet, G., Fournier, F., Legeais, J. F.,
 422 ... Picot, N. (2019, aug). On the resolutions of ocean altimetry maps. *Ocean*
 423 *Science*, 15(4), 1091–1109. doi: 10.5194/os-15-1091-2019
- 424 Balwada, D., Smith, K. S., & Abernathey, R. (2018, sep). Submesoscale Vertical
 425 Velocities Enhance Tracer Subduction in an Idealized Antarctic Circumpolar
 426 Current. *Geophysical Research Letters*, 45(18), 9790–9802. Retrieved from
 427 <https://agupubs.onlinelibrary.wiley.com/doi/10.1029/2018GL079244>
 428 doi: 10.1029/2018GL079244
- 429 Balwada, D., Xiao, Q., Smith, S., Abernathey, R., & Gray, A. R. (2021, jun). Vertical
 430 fluxes conditioned on vorticity and strain reveal submesoscale ventilation.
 431 *Journal of Physical Oceanography*. doi: 10.1175/jpo-d-21-0016.1
- 432 Barkan, R., Molemaker, M. J., Srinivasan, K., McWilliams, J. C., & D'asaro,
 433 E. A. (2019, jun). The role of horizontal divergence in submesoscale
 434 frontogenesis. *Journal of Physical Oceanography*, 49(6), 1593–1618. doi:
 435 10.1175/JPO-D-18-0162.1
- 436 Berta, M., Griffa, A., Haza, A. C., Horstmann, J., Huntley, H. S., Ibrahim, R.,
 437 ... Poje, A. C. (2020, oct). Submesoscale Kinematic Properties in Sum-
 438 mer and Winter Surface Flows in the Northern Gulf of Mexico. *Journal of*
 439 *Geophysical Research: Oceans*, 125(10), e2020JC016085. Retrieved from
 440 <https://agupubs.onlinelibrary.wiley.com/doi/10.1029/2020JC016085>
 441 doi: 10.1029/2020JC016085
- 442 Bol, R., Henson, S. A., Rumyantseva, A., & Briggs, N. (2018, dec). High-
 443 Frequency Variability of Small-Particle Carbon Export Flux in the North-
 444 east Atlantic. *Global Biogeochemical Cycles*, 32(12), 1803–1814. doi:
 445 10.1029/2018GB005963
- 446 Bopp, L., Resplandy, L., Orr, J. C., Doney, S. C., Dunne, J. P., Gehlen, M., ...
 447 Vichi, M. (2013). Multiple stressors of ocean ecosystems in the 21st century:
 448 Projections with CMIP5 models. *Biogeosciences*, 10(10), 6225–6245. doi:
 449 10.5194/bg-10-6225-2013
- 450 Boyd, P. W., Claustre, H., Levy, M., Siegel, D. A., & Weber, T. (2019). Multi-
 451 faceted particle pumps drive carbon sequestration in the ocean. *Nature*,
 452 568(7752), 327–335. doi: 10.1038/s41586-019-1098-2
- 453 Buckingham, C. E., Naveira Garabato, A. C., Thompson, A. F., Brannigan, L.,
 454 Lazar, A., Marshall, D. P., ... Belcher, S. E. (2016). Seasonality of sub-
 455 mesoscale flows in the ocean surface boundary layer. *Geophysical Research*
 456 *Letters*, 43(5), 2118–2126. doi: 10.1002/2016GL068009
- 457 Burd, A. B., Hansell, D. A., Steinberg, D. K., Anderson, T. R., Arístegui, J., Baltar,
 458 F., ... Tanaka, T. (2010, aug). Assessing the apparent imbalance between
 459 geochemical and biochemical indicators of meso- and bathypelagic biological
 460 activity: What the @\\$! is wrong with present calculations of carbon budgets?
 461 *Deep-Sea Research Part II: Topical Studies in Oceanography*, 57(16), 1557–
 462 1571. doi: 10.1016/j.dsr2.2010.02.022
- 463 Callies, J., Ferrari, R., Klymak, J. M., & Gula, J. (2015). Seasonality in subme-
 464 soscale turbulence. *Nature Communications*, 6(1), 6862. Retrieved from
 465 <https://doi.org/10.1038/ncomms7862> doi: 10.1038/ncomms7862
- 466 Cao, H., & Jing, Z. (2022, feb). Submesoscale ageostrophic motions within and be-

- 467 low the mixed layer of the northwestern Pacific Ocean. *Journal of Geophysical*
 468 *Research: Oceans*. Retrieved from <https://onlinelibrary.wiley.com/doi/10.1029/2021JC017812> doi: 10.1029/2021JC017812
- 470 Capet, X., Campos, E. J., & Paiva, A. M. (2008, aug). Submesoscale activity over
 471 the Argentinian shelf. *Geophysical Research Letters*, 35(15), L15605. Retrieved from <http://doi.wiley.com/10.1029/2008GL034736> doi: 10.1029/2008GL034736
- 474 Chelton, D. B., Schlax, M. G., & Samelson, R. M. (2011, oct). Global observations
 475 of nonlinear mesoscale eddies. *Progress in Oceanography*, 91(2), 167–216. doi:
 476 10.1016/j.pocean.2011.01.002
- 477 de Boyer Montégut, C., Madec, G., Fischer, A. S., Lazar, A., & Iudicone, D. (2004,
 478 dec). Mixed layer depth over the global ocean: An examination of profile data
 479 and a profile-based climatology. *Journal of Geophysical Research*, 109(C12),
 480 C12003. Retrieved from <http://doi.wiley.com/10.1029/2004JC002378> doi:
 481 10.1029/2004JC002378
- 482 Fox-Kemper, B., Adcroft, A., Böning, C. W., Chassignet, E. P., Curchitser, E.,
 483 Danabasoglu, G., ... Yeager, S. G. (2019, feb). *Challenges and prospects*
 484 in ocean circulation models
- (Vol. 6) (No. FEB). Frontiers Media S.A. doi: 10.3389/fmars.2019.00065
- 485 Freilich, M., & Mahadevan, A. (2021, may). Coherent Pathways for Subduction
 486 From the Surface Mixed Layer at Ocean Fronts. *Journal of Geophysical Research: Oceans*, 126(5), e2020JC017042. Retrieved from
 487 <https://onlinelibrary.wiley.com/doi/10.1029/2020JC017042> doi:
 488 10.1029/2020JC017042
- 489 Fu, L. L., & Ubelmann, C. (2014, feb). On the transition from profile altimeter to
 490 swath altimeter for observing global ocean surface topography. *Journal of Atmospheric and Oceanic Technology*, 31(2), 560–568. doi: 10.1175/JTECH-D-13-
 491 -00109.1
- 492 Gula, J., Molemaker, J. J., & Mcwilliams, J. C. (2014). Submesoscale cold filaments
 493 in the Gulf Stream. *Journal of Physical Oceanography*, 44(10), 2617–2643. doi:
 494 10.1175/JPO-D-14-0029.1
- 495 Gula, J., Taylor, J., Shcherbina, A., & Mahadevan, A. (2021, jan). Submesoscale
 496 processes and mixing. In *Ocean mixing: Drivers, mechanisms and impacts* (pp.
 497 181–214). Elsevier. doi: 10.1016/B978-0-12-821512-8.00015-3
- 498 Gula, J., Theetten, S., Cambon, G., & Roullet, G. (2021, June). *Description of the*
 499 *gigatl simulations*. Zenodo. Retrieved from <https://doi.org/10.5281/zenodo.4948523> doi: 10.5281/zenodo.4948523
- 500 J. J. Becker D. T. Sandwell, W. H. F. S. J. B. B. B. J. D. D. F. J. F. S. I. S.-
 501 H. K. R. L. K. M. S. N. A. P. R. T. J. V. R. G. W., & Weatherall, P. (2009).
 502 Global Bathymetry and Elevation Data at 30 Arc Seconds Resolution:
 503 SRTM30.PLUS. *Marine Geodesy*, 32(4), 355–371. Retrieved from <https://doi.org/10.1080/01490410903297766> doi: 10.1080/01490410903297766
- 504 Klein, P., & Lapeyre, G. (2009). *The oceanic vertical pump induced by mesoscale*
 505 *and submesoscale turbulence* (Vol. 1). doi: 10.1146/annurev.marine.010908-
 506 .163704
- 507 Lacour, L., Briggs, N., Claustre, H., Ardyna, M., & Dall'Olmo, G. (2019, mar). The
 508 Intraseasonal Dynamics of the Mixed Layer Pump in the Subpolar North At-
 509 lantic Ocean: A Biogeochemical-Argo Float Approach. *Global Biogeochemical*
 510 *Cycles*, 33(3), 266–281. doi: 10.1029/2018GB005997
- 511 Lapeyre Guillaume, K. P. (2006). *Impact of the small-scale elongated filaments*
 512 *on the oceanic vertical pump* (Vol. 64) (Article No. 6). FRANCE. Retrieved
 513 from <https://archimer.ifremer.fr/doc/00000/2459/> doi: <https://doi.org/10.1357/002224006779698369>
- 514 Large, W. G., McWilliams, J. C., & Doney, S. C. (1994, nov). Oceanic ver-
 515 tical mixing: A review and a model with a nonlocal boundary layer pa-

- 522 parameterization. *Reviews of Geophysics*, 32(4), 363. Retrieved from
 523 <http://doi.wiley.com/10.1029/94RG01872> doi: 10.1029/94RG01872
- 524 Le Corre, M., Gula, J., & Tréguier, A. M. (2020, apr). Barotropic vorticity bal-
 525 ance of the North Atlantic subpolar gyre in an eddy-resolving model. *Ocean*
 526 *Science*, 16(2), 451–468. doi: 10.5194/os-16-451-2020
- 527 Lévy, M., Couespel, D., Haëck, C., Keerthi, M., Mangolte, I., & Prend, C. J.
 528 (2024). The Impact of Fine-Scale Currents on Biogeochemical Cycles in
 529 a Changing Ocean. *Annual Review of Marine Science*, 16(1), 1–25. doi:
 530 10.1146/annurev-marine-020723-020531
- 531 Lévy, M., Franks, P. J., & Smith, K. S. (2018, dec). *The role of submesoscale cur-
 532 rents in structuring marine ecosystems* (Vol. 9) (No. 1). Nature Publishing
 533 Group. doi: 10.1038/s41467-018-07059-3
- 534 Llort, J., Langlais, C., Matear, R., Moreau, S., Lenton, A., & Strutton, P. G. (2018).
 535 Evaluating Southern Ocean Carbon Eddy-Pump From Biogeochemical-Argo
 536 Floats. *Journal of Geophysical Research: Oceans*, 123(2), 971–984. doi:
 537 10.1002/2017JC012861
- 538 Mahadevan, A. (2016, jan). The Impact of Submesoscale Physics on Primary
 539 Productivity of Plankton. *Annual Review of Marine Science*, 8(1), 161–184.
 540 Retrieved from [https://www.annualreviews.org/doi/10.1146/annurev-marine-010814-015912](https://www.annualreviews.org/doi/10.1146/annurev-

 541 -marine-010814-015912) doi: 10.1146/annurev-marine-010814-015912
- 542 Mahadevan, A., Pascual, A., Rudnick, D. L., Ruiz, S., Tintoré, J., & D’Asaro, E.
 543 (2020, jan). Coherent pathways for vertical transport from the surface ocean
 544 to interior. *Bulletin of the American Meteorological Society*, 101(11), E1996–
 545 E2004. doi: 10.1175/BAMS-D-19-0305.1
- 546 Mahadevan, A., & Tandon, A. (2006). An analysis of mechanisms for submesoscale
 547 vertical motion at ocean fronts. *Ocean Modelling*, 14(3-4), 241–256. doi: 10
 548 .1016/j.ocemod.2006.05.006
- 549 McWilliams, J. C. (2016, may). *Submesoscale currents in the ocean* (Vol. 472) (No.
 550 2189). Royal Society of London. doi: 10.1098/rspa.2016.0117
- 551 McWilliams, J. C. (2021, jan). Oceanic Frontogenesis. *Annual Review of Marine
 552 Science*, 13(1), 227–253. Retrieved from [https://www.annualreviews.org/
 554 doi/10.1146/annurev-marine-032320-120725](https://www.annualreviews.org/

 553 doi/10.1146/annurev-marine-032320-120725) doi: 10.1146/annurev-marine
 -032320-120725
- 555 Olafsson, J., Olafsdottir, S. R., Takahashi, T., Danielsen, M., & Arnarson, T. S.
 556 (2021, mar). Enhancement of the North Atlantic CO₂sink by Arctic Waters.
 557 *Biogeosciences*, 18(5), 1689–1701. doi: 10.5194/bg-18-1689-2021
- 558 Omand, M. M., D’Asaro, E. A., Lee, C. M., Perry, M. J., Briggs, N., Cetinić, I.,
 559 & Mahadevan, A. (2015). Eddy-driven subduction exports particulate or-
 560 ganic carbon from the spring bloom. *Science*, 348(6231), 222–225. doi:
 561 10.1126/science.1260062
- 562 Pietri, A., Capet, X., D’ovidio, F., Levy, M., Sommer, J. L., Molines, J. M., &
 563 Giordani, H. (2021, mar). Skills and limitations of the adiabatic omega equa-
 564 tion: How effective is it to retrieve oceanic vertical circulation at mesoscale
 565 and submesoscale? *Journal of Physical Oceanography*, 51(3), 931–954. doi:
 566 10.1175/JPO-D-20-0052.1
- 567 Ratner, B. (2009, jun). The correlation coefficient: Its values range between 1/1,
 568 or do they. *Journal of Targeting, Measurement and Analysis for Marketing*,
 569 17(2), 139–142. doi: 10.1057/jt.2009.5
- 570 Rocha, C. B., Gille, S. T., Chereskin, T. K., & Menemenlis, D. (2016, nov). Sea-
 571 sonality of submesoscale dynamics in the Kuroshio Extension. *Geophysical Re-
 572 search Letters*, 43(21), 11,304–11,311. doi: 10.1002/2016GL071349
- 573 Saha, S., Moorthi, S., Pan, H.-L., Wu, X., Wang, J., Nadiga, S., ... Goldberg, M.
 574 (2010). The NCEP Climate Forecast System Reanalysis. *Bulletin of the*
 575 *American Meteorological Society*, 91(8), 1015–1058. Retrieved from [https://
 journals.ametsoc.org/view/journals/bams/91/8/2010bams3001_1.xml](https://

 576 journals.ametsoc.org/view/journals/bams/91/8/2010bams3001_1.xml)

- doi: <https://doi.org/10.1175/2010BAMS3001.1>
- Shchepetkin, A. F., & McWilliams, J. C. (2005). The regional oceanic modeling system (ROMS): A split-explicit, free-surface, topography-following-coordinate oceanic model. *Ocean Modelling*, 9(4). doi: 10.1016/j.ocemod.2004.08.002
- Shcherbina, A. Y., D'Asaro, E. A., Lee, C. M., Klymak, J. M., Molemaker, M. J., & McWilliams, J. C. (2013, sep). Statistics of vertical vorticity, divergence, and strain in a developed submesoscale turbulence field. *Geophysical Research Letters*, 40(17), 4706–4711. Retrieved from <http://doi.wiley.com/10.1002/grl.50919> doi: 10.1002/grl.50919
- Siegelman, L., Klein, P., Rivière, P., Thompson, A. F., Torres, H. S., Flexas, M., & Menemenlis, D. (2020, jan). Enhanced upward heat transport at deep submesoscale ocean fronts. *Nature Geoscience*, 13(1), 50–55. doi: 10.1038/s41561-019-0489-1
- Siegelman, L. I. (2020, mar). Energetic submesoscale dynamics in the ocean interior. *Journal of Physical Oceanography*, 50(3), 727–749. doi: 10.1175/JPO-D-19-0253.1
- Stukel, M. R., Aluwihare, L. I., Barbeau, K. A., Chekalyuk, A. M., Goericke, R., Miller, A. J., ... Landry, M. R. (2017, feb). Mesoscale ocean fronts enhance carbon export due to gravitational sinking and subduction. *Proceedings of the National Academy of Sciences of the United States of America*, 114(6), 1252–1257. Retrieved from <https://pnas.org/doi/full/10.1073/pnas.1609435114> doi: 10.1073/pnas.1609435114
- Takahashi, T., Sutherland, S. C., Sweeney, C., Poisson, A., Metzl, N., Tilbrook, B., ... Nojiri, Y. (2002, jan). Global sea-air CO₂ flux based on climatological surface ocean pCO₂, and seasonal biological and temperature effects. *Deep-Sea Research Part II: Topical Studies in Oceanography*, 49(9-10), 1601–1622. doi: 10.1016/S0967-0645(02)00003-6
- Taylor, R. (1990, jan). Interpretation of the Correlation Coefficient: A Basic Review. *Journal of Diagnostic Medical Sonography*, 6(1), 35–39. doi: 10.1177/875647939000600106
- Treguier, A. M., Theetten, S., Chassignet, E. P., Penduff, T., Smith, R., Talley, L., ... Böning, C. (2005, may). The North Atlantic subpolar gyre in four high-resolution models. *Journal of Physical Oceanography*, 35(5), 757–774. doi: 10.1175/JPO2720.1
- Uchida, T., Balwada, D., Abernathey, R., McKinley, G., Smith, S., & Lévy, M. (2019, dec). The Contribution of Submesoscale over Mesoscale Eddy Iron Transport in the Open Southern Ocean. *Journal of Advances in Modeling Earth Systems*, 11(12), 3934–3958. Retrieved from <https://agupubs.onlinelibrary.wiley.com/doi/10.1029/2019MS001805> doi: 10.1029/2019MS001805
- Vic, C., Hascoët, S., Gula, J., Huck, T., & Maes, C. (2022). Oceanic Mesoscale Cyclones Cluster Surface Lagrangian Material. *Geophysical Research Letters*, 49(4), e2021GL097488. Retrieved from <https://agupubs.onlinelibrary.wiley.com/doi/abs/10.1029/2021GL097488> doi: <https://doi.org/10.1029/2021GL097488>
- Wenegrat, J. O., Thomas, L. N., Sundermeyer, M. A., Taylor, J. R., D'Asaro, E. A., Klymak, J. M., ... Lee, C. M. (2020, jul). Enhanced mixing across the gyre boundary at the Gulf Stream front. *Proceedings of the National Academy of Sciences of the United States of America*, 117(30), 17607–17614. doi: 10.1073/pnas.2005558117

627 Appendix A Figures

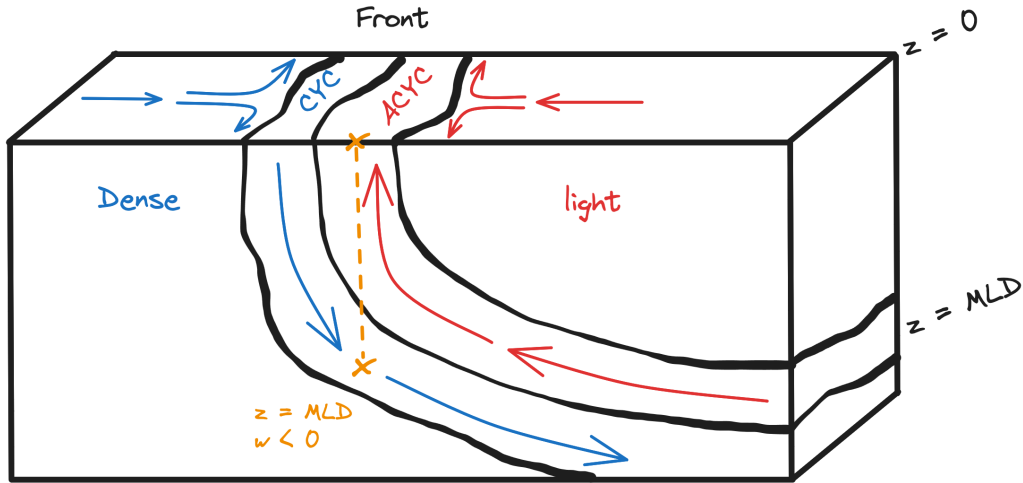


Figure A1. Scheme of a front cross-section. The orange cross represent the observation point. In this particular case, the vertical velocity below the surface anticyclonic front is not associated to an upwelling at $z=\text{MLD}$ due to the front slope. This lead to bias in our statistical results around and below the MLD.

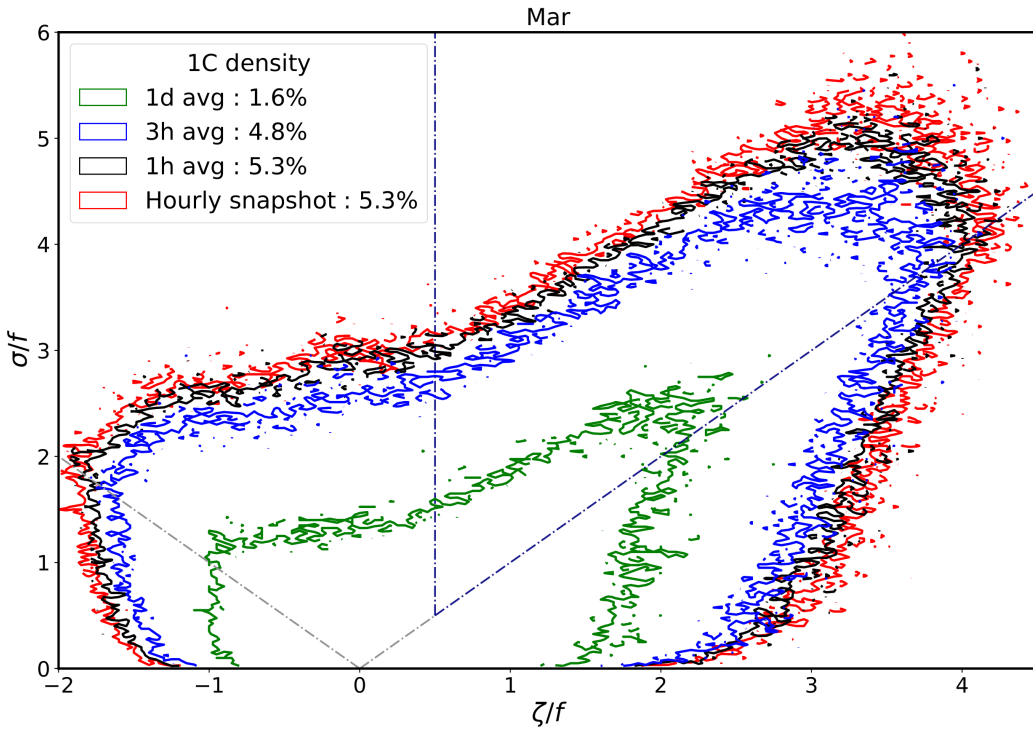


Figure A2. Surface strain-vorticity JPDF for 4 different outputs types which are daily averaged (green), 3-hour averaged (blue), 1h-averaged (black) and hourly snapshot (red). Black contour is the integrated domain that contain 99.99% of points. The fraction of points inside 1C are computed for each JPDF.